INTERNATIONAL JOURNAL OF HYDROGEN ENERGY 42 (2017) 20923–20933

Available online at www.sciencedirect.com

ScienceDirect

journal homepage: www.elsevier.com/locate/he

The effect of a Lorentz-force-driven rotating flow on the detachment of gas bubbles from the electrode surface

Tom Weier [a,*,1], Dominik Baczyzmalski [b,**,1], Julian Massing [b], Steffen Landgraf [a], Christian Cierpka [c]

[a] Helmholtz-Zentrum Dresden – Rossendorf, Bautzner Landstraße 400, 01328 Dresden, Germany
[b] Institut für Strömungsmechanik und Aerodynamik, Universität der Bundeswehr München, 85577 Neubiberg, Germany
[c] Institut für Thermodynamik und Strömungsmechanik, Technische Universität Ilmenau, 98693 Ilmenau, Germany

ARTICLE INFO

Article history:
Received 2 June 2017
Received in revised form
3 July 2017
Accepted 5 July 2017
Available online 22 July 2017

Keywords:
Electrolysis
Magnetohydrodynamics

ABSTRACT

The enhanced bubble detachment in water electrolysis due to Lorentz-forces is discussed for the case of mainly parallel electric and magnetic fields. Experiments and numerical simulations were carried out to assess the velocity and pressure distribution around single rigid spheres mimicking electrolytic bubbles on a horizontal electrode in the presence of a vertical magnetic field. Astigmatism particle tracking velocimetry delivered the three-dimensional flow field and a finite volume method was used for the computations. Formerly it was assumed that the flow-induced pressure decrease at the bubble's top caused the earlier detachment under magnetic field action. However, the experimental and numerical results obtained here demonstrate that this pressure decrease is too weak as to effectively change the detachment process. Finally, an alternative explanation for the observed bubble behavior is suggested: it might result from the comparatively strong global flow generated by the additive effect of a group of bubbles.

© 2017 Hydrogen Energy Publications LLC. Published by Elsevier Ltd. All rights reserved.

Introduction

Currently, water electrolysis constitutes only 4% of the world hydrogen production, while the major part is generated from fossil fuels [1]. The generation of hydrogen from natural gas is with 1 Euro/kg much cheaper than its production by water electrolysis with approximately 6–10 Euro/kg. However, the possibility to power water electrolysis by renewable energy sources without producing greenhouse gases will eventually make this technique competitive in the future. Moreover, hydrogen is an excellent energy carrier with a high energy density and can be easily reconverted into electrical energy in a fuel cell. Thus, water electrolysis is considered as a key technology for an efficient energy management, which will be important in an energy economy that mainly depends on renewable sources. Among the different electrolyzer types that exist today, alkaline water electrolysis is the most mature

* Corresponding author.
** Corresponding author.
E-mail addresses: t.weier@hzdr.de (T. Weier), dominik.baczyzmalski@unibw.de (D. Baczyzmalski).
[1] First and second author contributed equally to the paper.
http://dx.doi.org/10.1016/j.ijhydene.2017.07.034
0360-3199/© 2017 Hydrogen Energy Publications LLC. Published by Elsevier Ltd. All rights reserved.

and robust technology. It provides long lifetimes and does not rely on expensive cell materials or the need for high temperature handling, which makes this technique currently the most suitable option for the large-scale hydrogen production [2].

The minimum voltage to satisfy the energy demand required for the chemical reactions is referred to as the reversible cell voltage and amounts to $U_{rev} = 1.23$ V at standard conditions (T = 298.15 K, p = 1 bar). However, in reality additional losses arise due to reaction kinetics at the electrodes and ohmic losses. The cell voltage U_{cell} then calculates to

$$U_{cell} = U_{rev} + I\sum R + \Delta U_{anode} + \Delta U_{cathode}, \quad (1)$$

with $I\sum R$ accounting for the ohmic losses and ΔU_{anode} and $\Delta U_{cathode}$ denoting the anodic and cathodic overpotential, respectively [3]. Current alkaline water electrolyzers reach efficiencies up to 80–90% for high pressure (30 bar) and elevated temperatures (80 °C) [1]. However, for water electrolysis at atmospheric pressure and room temperature the efficiency reaches only 61–79%, depending on the effort taken for improving the performance. Particularly, at high current densities, i.e. high hydrogen production rates, the hydrogen and oxygen gas bubbles that are electrolytically generated at the respective electrodes significantly contribute to these losses, thus limiting the efficiency of the process and the operational current density [4]. As the void fraction in the cell becomes high with increasing current density, the effective conductivity of the bubble-filled electrolyte decreases and causes considerable ohmic losses [5,6]. On the other hand, since large parts of the electrode surface are covered by growing gas bubbles, the active electrode area is reduced and the entire current has to pass through the remaining parts of the electrode, which leads to high reaction overpotentials [7,8]. Therefore, reducing both the electrode bubble coverage and the void fraction is essential to minimize the bubble-related losses and allow for higher efficiencies and hydrogen production rates. It has long been recognized that electrolyte motion can be useful to accelerate the transport of bubbles away from the interelectrode gap, thus decreasing the void fraction and the corresponding ohmic losses [5,6,9,10]. In addition, it also helps to facilitate the bubble detachment and reduce the electrode bubble coverage [11,12]. A simple and inexpensive method to generate electrolyte motion very close to the electrodes in order to enable an earlier bubble detachment is the application of magnetic fields. The superposition of a magnetic field and the inherent electric field produces Lorentz-forces $\mathbf{F} = \mathbf{j} \times \mathbf{B}$, where $\mathbf{j}$ denotes the current density and $\mathbf{B}$ is the magnetic induction, respectively. These Lorentz-forces act directly as body forces in the fluid (electrolyte) and will generate electrolyte convection if they cannot be balanced by pressure.

The flow generated by an electrode-parallel magnetic field was shown to effectively reduce the void fraction in the interelectrode gap and lower the bubble coverage on large electrodes with increasing magnitude of the magnetic field [13–15]. Moreover, a reduction of the ohmic losses and overpotentials as well as an improved process performance were reported for the magnetic field [16–18]. Koza et al. [15,19,20] investigated the effect of both an electrode-parallel and electrode-normal magnetic field at large planar electrodes and showed that both configurations were able to reduce the bubble detachment size and the fractional bubble coverage on the electrode. The earlier bubble detachment in an electrode-parallel magnetic field can be attributed to the strong shear flow generated by the Lorentz-forces [21–24]. However, the underlying mechanisms occurring in an electrode-normal field are currently still under discussion [25,26]. When an electrode-normal magnetic field is applied, the resulting Lorentz-force is zero in regions where the electric field and the magnetic field are parallel. Now, since a bubble acts as an electric insulator it causes a non-homogeneous current density distribution in its close proximity as schematically shown in Fig. 1a. This induces Lorentz-forces in azimuthal direction which drive a rotating flow around the bubble. Since the curvature of the electric field lines changes in sign in the lower part, the Lorentz-force will act in opposite direction above and below the bubble's equator. Moreover, the electrical field lines are stronger distorted on the upper part of the bubble, which leads to slightly stronger Lorentz-forces than close to the bottom. Thus, the Lorentz-force-driven rotating flow can be generally expected to be faster above the bubble equator than below. To explain the faster detachment of the bubbles in such a configuration, it was suggested that the resulting flow

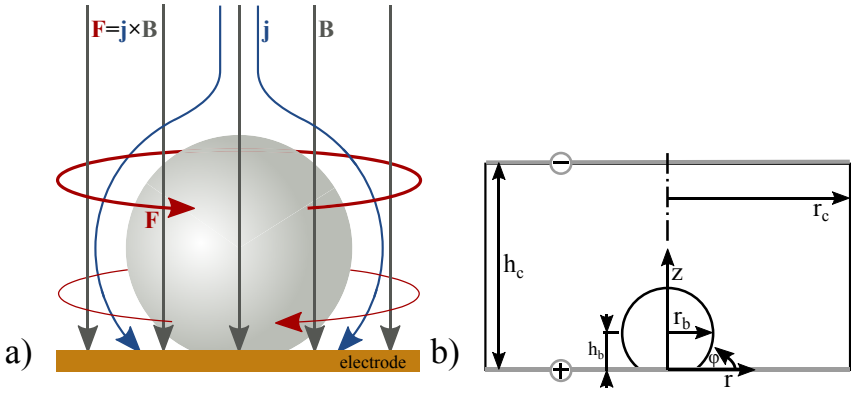

Fig. 1 – Sketch of the distribution of magnetic induction (B), current density (j), and Lorentz-force density (F) in the vicinity of an electrolytic bubble in an electrode-normal magnetic field (a). Coordinate system and designations of the problem (b).

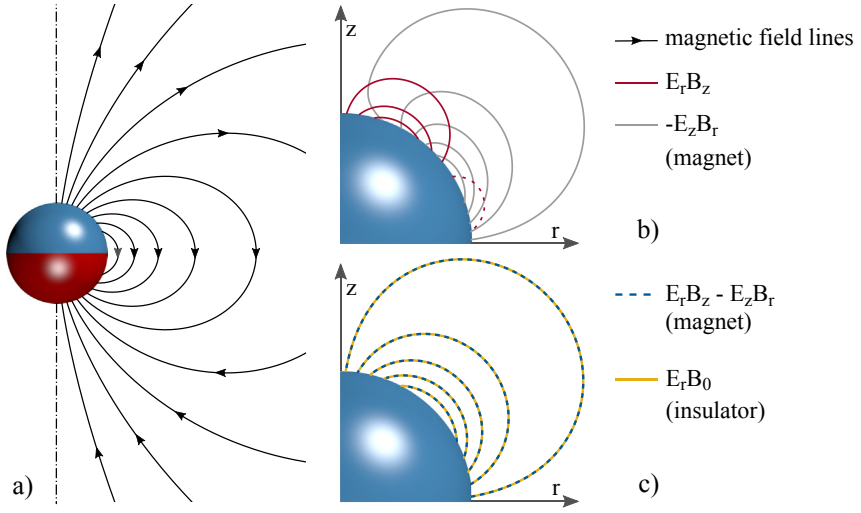

Fig. 2 – Magnetic field lines around the magnetized sphere in the meridional plane (a), single terms of the cross product describing the Lorentz force for the magnetized sphere (b; contour lines, negative values of E_rB_z are dashed), and comparison of the Lorentz force contours for the magnetized sphere and the insulating sphere with external field (c).

forms a region of lower pressure above the bubble. This imposes a force acting in favor of the bubble detachment and thus could explain the reduced detachment size observed in the electrode-normal magnetic field [15].

To pursue this assumption and gain further insight on how to optimize the magnetic field arrangements, a better understanding of the complex three-dimensional flow around the evolving bubbles is necessary. However, it is almost impossible to experimentally investigate the flow around real individual bubbles growing on large electrode since many bubbles may form simultaneously at random places all over the electrode. An alternative approach chosen by many researches is to use nano- [27] or microelectrodes (diameter ~O(100 μm)) in order to pin the bubbles at a certain position which can be investigated by optical means [26,28–31]. In contrast to the observations at large electrodes, the experimental and numerical results reported in these studies point to a stabilizing effect of the electrode-normal magnetic field, i.e. an increase of the detachment size. The opposite behavior can be attributed to the strong difference of the Lorentz-force distribution. Since the entire current has to pass through the much smaller microelectrode, the current density and the Lorentz-forces are much stronger at the bottom than at the top of the bubble. This gives rise to a lower pressure in the lower part of the bubble as opposed to the case at large electrodes and may explain the stabilizing effect [25,26]. Therefore, the reported gas bubble behavior on microelectrodes cannot be directly transferred to the realistic case of gas bubbles on macroelectrodes as the Lorentz-force distributions in both cases are by no means comparable.

The aim of the current study is to provide further insight into the complex flow generated by an electrode-normal magnetic field and clarify the effect of the hydrodynamic force on the bubble detachment at large electrodes. Since the bubbles form at random places it is not possible to conduct detailed flow measurements around a single bubble at a large electrode, therefore a magnetized sphere is used here instead. This setup enables to mimic a single stationary electrolytic gas bubble on a macroelectrode with an equivalent Lorentz-force distribution. The three-dimensional electrolyte flow around the magnetic sphere was experimentally resolved for the first time using Astigmatism Particle Tracking Velocimetry. These measurements are supported by additional numerical simulations, which allowed for the calculation of the hydrodynamic forces that are imposed on the sphere or bubble by the Lorentz-force-driven flow. In addition, Particle Image Velocimetry (PIV) measurements were conducted in a second setup employing an arrangement of multiple magnets in order to study the global flow that develops around a group of bubbles as opposed to a single bubble.

Experimental setup

Given the rotational symmetry of the Lorentz-force-driven flow around a single sphere in an electrode-normal magnetic field (see Fig. 1a), a cylindrical electrolysis cell with an inner diameter of 35.6 mm was used for the measurements as shown in Fig. 3. The cell was made from Plexiglass to allow for optical access for illumination from the side walls. The working electrode consists of pure copper and formed the

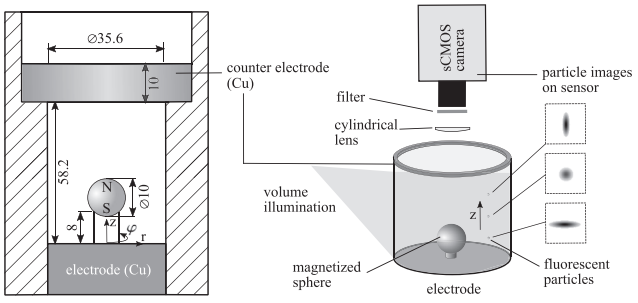

Fig. 3 – Sketch of the electrochemical cell employing a magnetized sphere (left) and the corresponding APTV measurement setup (right).

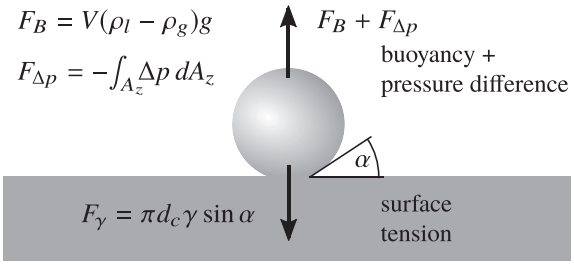

Fig. 4 – Sketch of the forces acting on a bubble at a horizontal electrode.

bottom of the cell, whereas a copper ring electrode placed on the top of the cell served as counter electrode. This allowed for an undisturbed observation of the measurement volume from the top. To avoid optical distortions due to the curved surface at the rim a transparent plastic sheet was placed on top of the free surface of the cell and ensured a flat upper surface. At the bottom of the cell an axially magnetized NdFeB sphere with a diameter of 10 mm was placed onto a plastic pillar with a height of 8 mm. Using this magnetized sphere the same Lorentz-force distribution as in the case of a stationary spherical gas bubble at a large electrode in an electrode-normal magnetic field can be generated as will be explained in the following. The magnetic field in an infinite domain outside ($r > r_b$) of a spherical magnet with magnetization M_0 is given by Ref. [32].

$$B_r = \frac{2}{3}M_0\frac{r_b^3}{r^3}\cos\theta,$$
$$B_\theta = \frac{1}{3}M_0\frac{r_b^3}{r^3}\sin\theta. \quad (2)$$

Here, r, θ, φ are spherical coordinates originating at the center of the sphere and r_b is the radius of the sphere (see Fig. 1b). Similarly, the electric field around a spherical insulator in an infinitely extended space can be written as [33].

$$E_r = E_0\left(1 - \frac{r_b^3}{r^3}\right)\cos\theta,$$
$$E_\theta = -E_0\left(1 + \frac{r_b^3}{2r^3}\right)\sin\theta. \quad (3)$$

From Eqs. (2) and (3) the Lorentz-force distribution around an electrically insulating spherical magnet results as

$$f_{L,M} = \sigma_e \mathbf{E} \times \mathbf{B} = \sigma_e E_0 M_0 \frac{r_b^3}{r^3}\sin\theta\cos\theta\,\mathbf{e}_\varphi. \quad (4)$$

On the other hand, the Lorentz-force distribution around and insulating (and non-magnetic) sphere in an uniform vertical magnetic field B_0 follows as

$$f_{L,B} = -\frac{3}{2}\sigma_e E_0 B_0 \frac{r_b^3}{r^3}\sin\theta\cos\theta\,\mathbf{e}_\varphi. \quad (5)$$

Note that the Lorentz-force distributions solely possess an azimuthal (φ) component and for both cases differ only by a constant factor. Identical Lorentz-force distributions for $f_{L,M}$ and $f_{L,B}$ result if

$$B_0 = -\frac{2}{3}M_0. \quad (6)$$

To illustrate the field distributions, Fig. 2a shows the magnetic field lines around a magnetized sphere in the right meridional half-plane. Contour lines of the single terms contributing to the azimuthal Lorentz-force density are displayed in Fig. 2b for the top right quarter of the magnet (the distributions in the other quadrants are symmetric). The terms are given in in-plane coordinates r,z. For a non-magnetic insulating sphere the Lorentz-force contours would simply trace the E_r contours since the z-parallel B_0 is constant everywhere. In contrast, for the magnetized sphere, the E_rB_z-term is relatively small and even becomes negative near the spheres' equator due to the sign change of B_z. This is, however, compensated by the $-E_zB_r$-term. Note that the latter is completely absent for an insulating sphere in an electrode normal magnetic field. Finally, Fig. 2c demonstrates the perfect identity of the Lorentz-force density contours around a magnetized and an insulating sphere provided condition (6) is fulfilled.

To obtain the same Lorentz-force distribution for an insulating sphere and a magnetized sphere requires electric field lines that are not distorted by the influence of the electrode. Therefore, the magnetized sphere could not be placed directly on the electrode but had to be lifted from the ground. The Lorentz-force distribution is generally confined to the vicinity of the sphere, although the ring electrode also creates strong distortions of the current field in the upper part of the cell. The magnetic field is already very weak in this region and thus the generated Lorentz-forces can be neglected. Since the elevated magnetic sphere cannot account for the effect of the bottom wall, the case of an insulating sphere directly attached to the electrode will be additionally considered in a second set of numerical simulations (see Sec. Numerical Simulations).

The cell was filled with a 1 M $CuSO_4$ solution as an electrolyte, which ensured in conjunction with the pure copper electrodes that an electric current is established even below the decomposition voltage of water. It should be mentioned that local density gradients will be created in the electrolyte with time due to the dissolution and deposition of copper. However, since the bottom electrode was used as the anode, copper was only dissolved at the bottom of the cell, which leads to a stable stratification. The experiments were carried out under galvanostatic conditions, i.e. using a constant current supply. Different values of the electric current were applied in successive experiments in order to vary the magnitude of the Lorentz-force ($f_L \sim jB$). Here, a current of $I = 30$, 60, 90, 120 and 150 mA was used, which yields a current density at the surface of the working electrode of about $j = 30$, 60, 90, 120 and 150 Am^{-2}. The magnetization of the sphere amounts to 1 T, thus generating a Lorentz-force distribution that is equivalent to that induced by an uniform electrode-normal magnetic field of $B_0 = 0.66$ T according to Eq. (6).

A sketch of the experimental setup is shown on the right side of Fig. 3. All three components of the three-dimensional velocity field (3D3C) around the elevated magnetized sphere were measured by means of Astigmatism Particle Tracking Velocimetry [APTV, see Ref. [34]]. This is a special single-camera particle tracking technique in which a cylindrical lens is placed in front of the camera to disturb the axis-symmetry of the optical system and causes astigmatic aberrations. The particle images will appear elliptical, where the size of the major and minor axes unambiguously depend on the actual

depth position in the measurement volume. The optical magnification changes with depth and was approximately 32 μm/pixel in the x-direction and 27 μm/pixel in the y-direction. By a proper image processing and calibration this can be correlated with the actual depth position of the particle [35]. With this method, the measurement uncertainty in determining the depth position of individual particle images was estimated to be approximately 3% (twice the standard deviation) of the measurement volume depth which corresponds to 1.2 mm. However, since the flow is steady the data could be time-averaged, which reduces the uncertainty by orders of magnitude. The uncertainty in determining the x- and y-position of the particle image is associated with the ability to accurately detect the particle image center, which is for the routines used here below 0.05 pixel [36]. This results in an uncertainty below 1.62 and 1.37 μm for individual particle positions in the x- and y-direction, respectively. Fluorescent polystyrene particles (FluoRed by Microparticles GmbH) with a diameter of 50 μm served as flow tracers. Even though these particles are relatively large, they do not suffer from fast sedimentation, since their density is very close to that of the electrolyte ($\rho_{CuSO4} \approx 1.05$ gcm^{-3}, $\rho_{particle} \approx 1.06$ gcm^{-3}). The sedimentation velocity was calculated to be 8 μm/s [37], which corresponds to below 0.2% of the mean absolute velocity in the axial direction. A pulsed Nd:YAG laser with a wave length of 532 nm and a pulse energy of 15 mJ was used as a light source. The laser beam was passed through a beam expander via an optical fiber and illuminated the entire cell. The images were captured from the top at a frame rate of 15 Hz by a sCMOS camera (Imager sCMOS, LaVision GmbH) and a Zeiss f = 50 mm macro-planar objective. Two laser pulses without time delay were shot in each frame, to increase the illumination intensity. A 532 nm notch filter was mounted on the objective to only transmit the fluorescent light emitted by the tracer particles and avoid the strong laser reflections from the copper surface. Moreover, a cylindrical lens with a focal length of f = 300 mm was placed in front of the camera to create astigmatic distortions of the particle images. The resulting measurement volume extended over the entire inner diameter of the electrolysis cell, from the bottom of the cell (z = 0 mm) to a height of z ≈ 40 mm. The velocity was reconstructed from the three-dimensional particle positions by determining the particle trajectories with a time-resolved tracking algorithm. Moreover, the trajectories were locally fitted by a second order polynomial fit for a higher accuracy [38]. This procedure also acts as a very efficient outlier detection since only trajectories with four or more particle positions were taken into account. Since the flow is steady and rotationally symmetric, the velocity data was averaged over the whole circumference into one meridional (rz) plane. The corresponding bin size was 0.5 × 0.5 mm^2.

Numerical simulations

The finite volume library OpenFOAM licensed under the GNU General Public Licence [39] was used to perform the computations. To incorporate the electromagnetic body force, the solver simpleFoam of OpenFOAM version 1.7. x was extended by a Lorentz-force term. Under the conditions considered here, this term can be pre-computed and does neither depend on time nor on the flow. This is not immediately clear from Ohm's law for moving conductors

$$\mathbf{j} = \sigma(\mathbf{E} + \mathbf{v} \times \mathbf{B}) \tag{7}$$

that - besides the conventional proportionality to the electric field $\mathbf{E}$ – relates the current density to an induction term $\mathbf{v} \times \mathbf{B}$ depending on velocity $\mathbf{v}$ and magnetic field $\mathbf{B}$. However, the electrolyte's electrical conductivity σ is quite small and velocities as well as magnetic field magnitudes are moderate. For this reason, the electric currents induced by the electrolyte motion and even more so the magnetic fields of the induced currents can safely be neglected compared to the applied electric and magnetic fields. Therefore, the calculation of the Lorentz-forces can be decoupled from solving the Navier-Stokes equations.

Current distributions were always determined numerically in order to account for additional insulating parts such as the pillar tethering the sphere, even if the analytical expression was used for the magnetic field of the magnetized sphere. The electric field $\mathbf{E}$ was computed by solving a Laplace equation for the electric potential using the OpenFOAM solver laplacianFoam. Fixed potentials were set at the top and the bottom of the cell such as to match the desired cell current. The vertical boundaries as well as the bubbles surface were treated as insulating, i.e., no normal currents were allowed there. The current density distribution then results simply from the gradients of the electric potential times conductivity.

Two slightly different setups were used for the comparison with the experiment (Figs. 5 and 6) on the one hand and to determine the scaling of the forces (Fig. 7) on the other hand. That means, the first configuration is based on the experiment using the tethered magnetized sphere as discussed in the previous section. Validated by the experimental data, these simulations formed the groundwork for the computation of the more bubble-growth-like case of an insulating sphere that is directly attached to the electrode. This way, the effect of the electrode on the current distribution and the influence of the solid wall on the flow can also be accounted for. For the latter case, a homogeneous magnetic field in vertical direction was combined with the electric field obtained from the Laplace equation.

In both cases, the two-dimensional Navier-Stokes equations with body force term were solved on an axis-symmetric structured grid. A mesh with approximately 2.5 × 10^5 hexahedral cells and highest resolution in the vicinity of the sphere was used for the tethered sphere geometry of Fig. 3. The parameter studies depicted in Fig. 7b were conducted under the assumption of a constant aspect ratio between cell and bubble, while the cell radius (r_c, Fig. 1b) amounted to four times the bubble radius and the cell height (h_c, Fig. 1b) was twelve times the radius of the bubble.

Results and discussion

Forces

The detachment of the bubble from the electrode surface depends on the forces that are acting on it. The prevailing forces

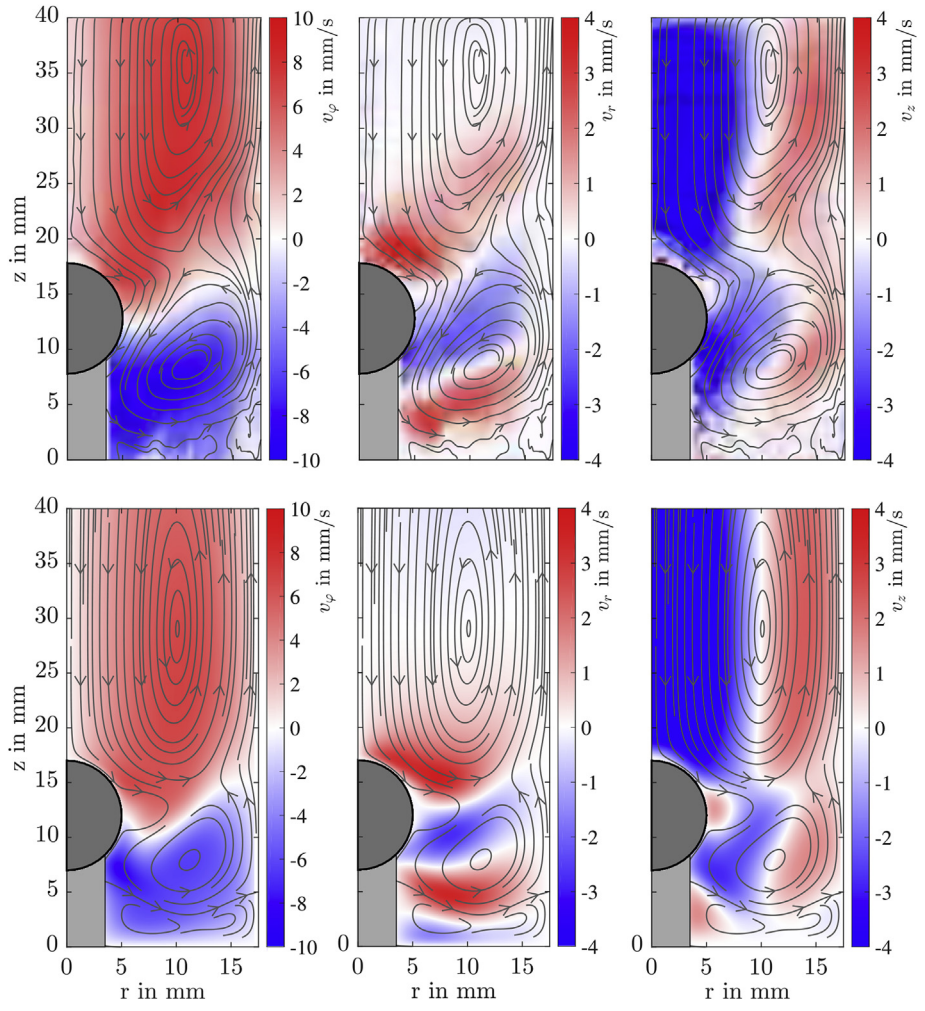

Fig. 5 – Experimentally (top) end numerically (bottom) obtained velocity field around the magnetized sphere in the *rz*-plane. The grid size for representation of the data is 0.5 mm and 0.25 mm in each direction for the experimental and numerical data, respectively. Circumferential velocity (left), radial velocity (middle) and axial velocity (right). The streamlines (grey) were added to better visualize the in-plane velocity field in the meridional (*rz*) plane.

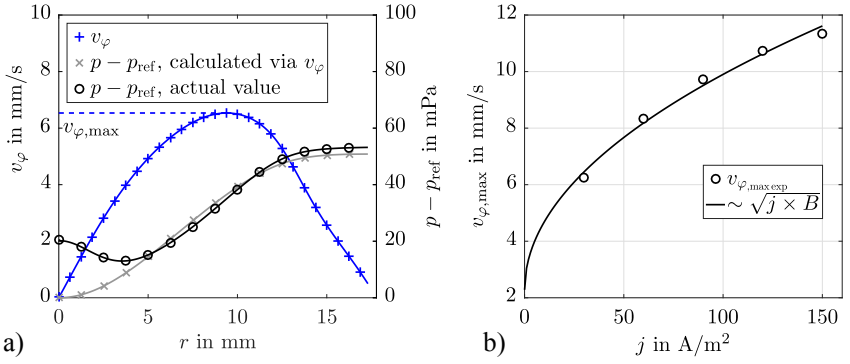

Fig. 6 – Radial distribution of v_φ and the relative pressure $p - p_{\mathrm{ref}}$ in a horizontal plane located 1 mm above the sphere obtained from the simulations at $j = 60$ A/m^2 (a). Maximum measured azimuthal velocity v_φ in the cell vs. the applied current density j (b).

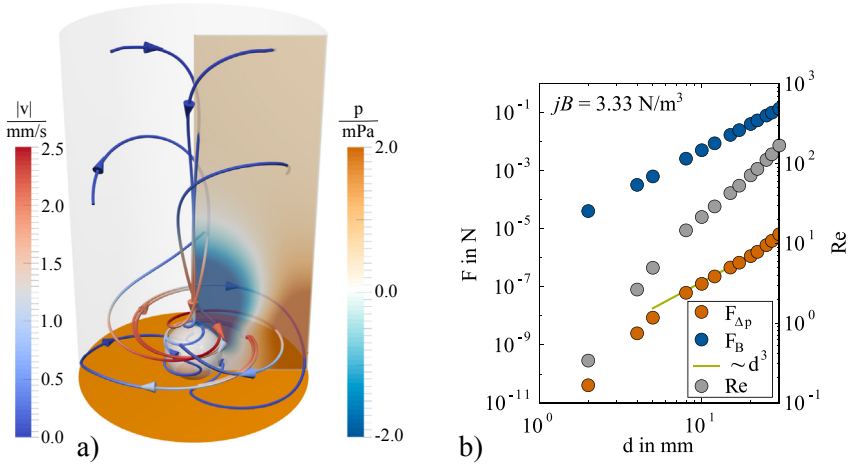

Fig. 7 – Lorentz-force-driven rotating flow around an insulating sphere obtained from numerical simulation with streamlines colored by the velocity magnitude and the pressure contour illustrated in the meridional plane (a). Hydrodynamic lift force, buoyancy and Reynolds number calculated for different diameters (b).

that are usually considered in this context are the buoyancy F_B, the surface tension force F_γ and the hydrodynamic forces, here referred to as $F_{\Delta p}$ (see Fig. 4). The buoyancy force acts in favor of the bubble detachment and increases with the bubble size according to

$$F_B = \left(\rho_l - \rho_g\right) V \; g = \left(\rho_l - \rho_g\right) \frac{\pi}{6} d^3 g, \tag{8}$$

where ρ_g and ρ_l, are the density of the gaseous phase (bubble) and the liquid phase (electrolyte), respectively, V denotes the bubble volume, d is the bubble diameter and g the gravitational acceleration. The surface tension force F_γ, on the other hand, is responsible for keeping the bubble attached to the surface. For the simple case of a bubble adhering to a horizontal surface in a rotationally symmetric flow, the resulting force can be written as

$$F_\gamma = -\pi d_c \gamma \sin\alpha, \tag{9}$$

where α denotes the contact angle, γ is the gas-liquid surface tension and d_c is the contact diameter of the bubble with the wall. Since a stationary sphere is considered here, no hydrodynamic drag is imposed. The only relevant hydrodynamic force that needs to be considered in the present case is related to the flow-induced relative pressure change along the surface of the sphere, which yields for the z-direction

$$F_{\Delta p} = -\int_{A_z} (p_l - p_c) dA_z, \tag{10}$$

where $\Delta p = p_l - p_c$ is the hydrodynamic pressure of the liquid relative to the reference pressure at the contact line and A_z is the bubble surface projected in z-direction. In a stagnant liquid the bubble will generally stay attached to the surface until the bubble size and thus its buoyancy becomes sufficiently large to overcome the surface tension force. In the presence of an electrode-normal magnetic field, the flow-induced pressure force $F_{\Delta p}$ might facilitate its detachment. Based on the numerical results $F_{\Delta p}$ will be compared to the buoyancy force F_B in order to assess the effect of the flow-induced pressure change on the bubble detachment.

Flow fields

The flow fields are qualitatively very similar for the different investigated currents. Therefore, only the flow field at $I = 60$ mA is considered here for a detailed discussion. Fig. 5 shows all three mean velocity components in the meridional (rz) plane together with stream lines of the secondary (in-plane) flow for the experiment (top) and the simulation (bottom). The azimuthal velocity v_φ is shown on the left, the radial velocity v_r in the middle and the axial/vertical velocity v_z on the right. As can be seen from the azimuthal velocity distribution (left side of Fig. 5), the experimental and numerical data is in very good agreement. As expected, the Lorentz-forces give rise to a rotating flow with different sign on the upper and lower side of the sphere. This is different to the case of a microelectrode, where the Lorentz forces are dominant on the lower side of the bubble due to the high current density and no counter-rotating flow could be observed on the upper side [26]. Since the magnetized sphere is elevated, the bending of the electric field lines is in the same order of magnitude on both sides of the sphere and thus the Lorentz forces are also relatively similar in this case. In the region of the sphere (8.5 mm $\leq z \leq$ 18.5 mm), the magnitude of the azimuthal flow above the sphere is indeed slightly larger (~ 10%) than in the lower part of the sphere as expected from the theoretical field distribution (Fig. 1). Furthermore, the average position of the shear layer between the counter-rotating flow regions is not horizontally aligned, but follows a curved path which is inclined upwards in radial direction and shows a minimum at $r = 7$ mm and $z = 10$ mm. It can be also seen that the Lorentz-force-induced flow is not limited to the vicinity of the sphere but the fluid rotates in the entire cell. Moreover, the azimuthal velocities increase with the applied current density as is shown in Fig. 6b for the maximum measured velocity in the cell. It can be seen that the maximum velocity increases

approximately with the square root of the current density, $v_\varphi \sim \sqrt{j}$, which can be attributed to the fact that the dynamic pressure is directly related to the imposed Lorentz forces, i.e. $\frac{\rho}{2}v_\varphi^2 \sim jBd$ (d is the diameter of the sphere representing a characteristic length scale).

The azimuthal fluid motion will obviously give rise to centrifugal forces, which in turn will cause the pressure to increase toward the outer wall. Since the azimuthal velocity is the predominant flow component, the pressure change can be estimated by

$$\frac{\partial p}{\partial r} = \rho \frac{v_\varphi^2}{r}. \tag{11}$$

This is exemplified in Fig. 6a, where the radial distribution of the azimuthal velocity and the corresponding relative pressure change are illustrated in a horizontal plane slightly above the sphere (numerical results). The relative pressure distribution obtained by integrating the velocity profile according to Eq. (11) is generally in good agreement with the distribution directly obtained from the numerical simulation. Differences occur within the inner region for $r < 5$ mm directly above the sphere due to the action of the secondary flow as discussed below.

In the middle and right column of Fig. 5 the secondary flow in the meridional plane is shown and additionally highlighted by the streamlines. Due to the centrifugal force caused by the azimuthal motion above and below the sphere, the fluid is forced to move toward the outer part of the cell as indicated by the red color in the representation of v_r. In the shear layer, where the azimuthal velocity and the centrifugal forces are rather small, the fluid flows back from the outer parts due to continuity. The numerical data shows that such inward directed flow is also evident close to the bottom of the cell. This can similarly be attributed to the low centrifugal momentum in the wall boundary layer which cannot withstand the elevated pressure in the outer cell region [see Ref. [40]]. Since measurements close to the wall are subjected to a higher noise level, this effect cannot be seen in the experimental data.

The distribution of the axial velocity v_z is again in very good agreement between the experimental and numerical results. Above the sphere a large flow region is directed toward the sphere (indicated by the blue color, $v_z \approx -5$ mms^{-1}). This is a consequence of the lower pressure in the center of the cell caused by the rotating motion. Due to the impingement of this flow on the upper part of the sphere the pressure reduction in this region is weaker compared to the case where only the action of azimuthal flow is considered as previously shown in Fig. 6a. After approaching the sphere the fluid is accelerated outwards due to the centrifugal forces as explained before. Finally, the fluid has to flow upwards at the outer part of the cell due to continuity. Since the available area becomes larger with increasing radius, the absolute velocity of the upward flow in the outer part is smaller ($v_z \approx 2$ mms^{-1}) compared to the downward flow in the inner part. It is also interesting to note that the portion of fluid moving downward along the sphere detaches from the sphere close to the equator at $r \approx 5$ mm and $z \approx 12$ mm, as indicated by the small region of upward moving motion. The resolution of the experimental data is high enough to show the same feature, although to a smaller extent.

The hydrodynamic lift force

As suggested by Koza et al. [15] the higher azimuthal flow velocities on the upper side of the sphere will lead to a lower pressure in comparison to the lower side of the bubble. The result of such a pressure distribution is a hydrodynamic lift force that may facilitate the bubble detachment. However, as was shown before in Fig. 6a the pressure change induced by the azimuthal fluid motion is relatively small (<50 mPa). By comparison, the hydrostatic pressure change around the sphere is $\Delta p = \rho g d \approx 100$ Pa. Thus, irrespective of the additional action of the secondary flow, the Lorentz-force-induced lift force can be expected to be several orders of magnitude lower than the buoyancy force. However, since the size of electrolytically generated hydrogen or oxygen gas bubbles is much smaller than that of the investigated sphere, it is important to understand how the respective forces scale with the diameter of the bubble. According to Eq. (11) the flow-induced pressure change can be written as $\Delta p \sim \rho v_\varphi^2$. Moreover, the velocity scales approximately with $v_\varphi \sim \sqrt{jBd}$ as discussed before (see also Fig. 6b). The flow-induced pressure change can be therefore related to the Lorentz forces by

$$\Delta p \sim \rho v_\varphi^2 \sim jBd. \tag{12}$$

The resulting pressure-induced lift force can be then estimated according to

$$F_{\Delta p} \sim \Delta p \frac{\pi}{4} d^2 \sim jBd^3. \tag{13}$$

Thus, the generated lift force scales with d^3. Now, since the buoyancy of a gas bubble ($F_B \sim (\rho_l - \rho_g) g d^3$) also scales with d^3, the ratio between the lift force and the buoyancy force can be expected to be independent of the bubble size in a first approximation.

To support these findings, the imposed lift force can be directly calculated from the numerical simulations. To include the effect of the electrode on the Lorentz force distribution and the flow, which was not correctly reproduced by the elevated magnetized sphere, the more realistic case of an insulating sphere directly attached to the electrode will be considered here. Fig. 7a shows the corresponding flow field, visualized by the three-dimensional streamlines colored by their velocity magnitude. In addition, pressure contours are shown in the meridional plane (rz-plane). The lift force $F_{\Delta p}$ calculated from this pressure distribution at different values of the sphere's diameter is shown in Fig. 7b together with the corresponding buoyancy force and the Reynolds number. The magnitude of the simulated Lorentz forces was relatively small ($f_L \sim jB = 3.33$ Nm^{-3}), but still exceeds that used in the parallel fields experiment of Koza et al. [15] by about an order of magnitude. As can be seen, the hydrodynamic lift force $F_{\Delta p}$ is in the order of 10^{-7} N for a diameter of 10 mm and is approximately four orders of magnitude lower than the buoyancy force. As expected from the discussion above, the $F_{\Delta p} \sim d^3$ dependency is generally evident. However, as the diameter is reduced the reduction of the lift force becomes

even stronger due to viscous effects which become more relevant at low Reynolds numbers. Consequently, the flow-induced lift force is unlikely to be the reason for the reduction of the bubble detachment diameter observed by Koza et al. [15] in an electrode-normal magnetic field.

On the other hand, for much higher current densities in the order of 10 kAm^{-2} and magnetic fields of $B \approx 1$ T ($jB = 10$ kNm^{-3}), which are realistic conditions for practical applications, the lift force may have a more significant contribution. However, at high current densities the bubble coverage on the electrode surface and the void fraction becomes very high, so that the interaction between the bubbles would also have to be taken into account. In fact, even at low current densities and minor electrode bubble coverage the interaction between the flow around the individual bubbles could lead to relevant effects as discussed in the next section.

Multiple magnets

Stretching the analogy between magnets and bubbles even further, this section deals with the flow driven by two different magnet arrays, one of them generating a Lorentz force distribution relatively similar to that arising around a group of bubbles attached to a horizontal electrode in a vertical magnetic field.

Fig. 8 shows two different arrangements of nine cylindrical permanent magnets made of NdFeB (Fig. 8a and d) fixated below a 0.5 mm thick Pt foil used as cathode. A single magnet had a diameter and height both of 3 mm. The cell's diameter and height were 40 mm and 50 mm, respectively. The cell was filled with an aqueous solution of 0.9 M $CuSO_4$ and 1.5 M H_2SO_4. Current flows from a 10 mm high Cu anode mounted to the inner rim on top of the cell towards the cathodic Pt plate on the bottom of the cell. The arrangement is quite similar to the setup shown in Fig. 3. Since the magnetic fields of the upper poles of the permanent magnets penetrate the Pt foil circumferential Lorentz-forces are generated atop of each single magnet as sketched between Fig. 8b and c. Depending on the magnetization direction, the Lorentz-force is directed either clockwise (north pole on top) or counter-clockwise (south pole on top).

For the following discussion, a coordinate system originating at the cells center at the upper surface of the Pt foil will be used. z is the vertical coordinate. The flow was measured with conventional PIV in horizontal slices of constant z. Therefore, the velocity magnitude ($|v|$) contains only velocity components in the horizontal plane. In the checkerboard arrangement (Fig. 8a, b, e, f) the forces generated by the single magnets add up in the inter-magnet spaces. Accordingly, a relatively regular flow develops directly above the magnet array at $z = 1$ mm (Fig. 8e) closely tracing the magnet contours. Slightly farther away from the cathode only a weak and barely detectable motion remains ($z = 5$ mm, Fig. 8f). Essentially, the checkerboard arrangement of the permanent magnets leads to a locally intense flow limited to the direct vicinity of the cathode. Further away some weak motions are still detectable, but no large scale flow is driven.

In contrast, an array of magnets with parallel magnetization directions (Fig. 8d) generates unidirectional rotation around the poles. In this case forces originating from the single magnets are opposing in the inter-magnetic spaces and partially cancel each other out (Fig. 8c). However, along the outer rim of the magnet array the Lorentz-forces from single magnets have the same (in the current case counter-clockwise) direction and add up. This situation is comparable to the summation of the magnetization currents in a volume, where only the surface magnetization currents contribute to the macroscopic field (c.f., e.g. Ref. [41]). The force configuration in Fig. 8d resembles that originating from a group of bubbles on a larger electrode. The direction of the azimuthal force around single bubbles is the same, so Lorentz-forces are weakened in the inter-bubble spaces but sum up around the bubble collective. Returning to the magnets, at $z = 1$ mm (Fig. 8g) the electrolyte flows around the array following roughly the counter-clockwise Lorentz-forces along the eight outer magnets. The rectangular shape of the

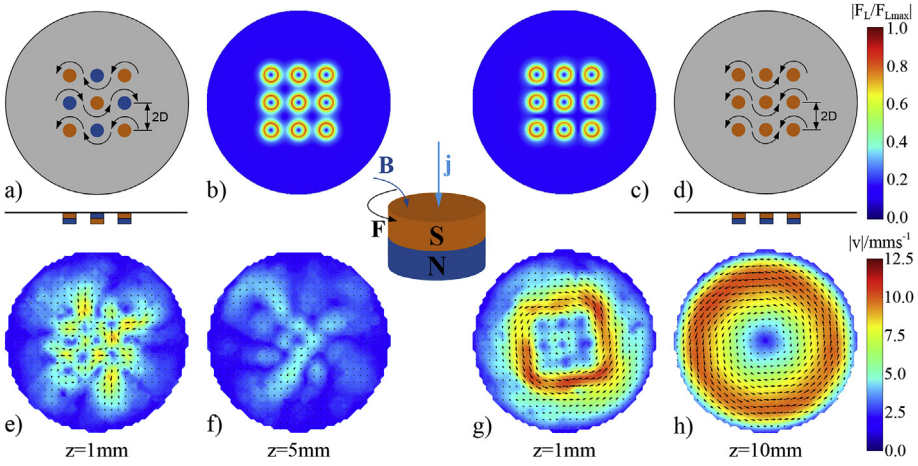

Fig. 8 – Lorentz-force distribution and flow generated by multiple magnets with magnetization directions all parallel (rightmost two columns) or in a checkerboard arrangement (leftmost two columns). A single magnet has a diameter $D = 3$ mm and a height $H = 3$ mm, the cell diameter and height are 40 mm and 50 mm, respectively. Current densities of 380 Am^{-2} and 360 Am^{-2} were applied to the checkerboard (e, f) and the parallel (g, h) arrangement, respectively.

maximum velocity contour is tilted somewhat in flow direction with respect to the magnet array. Inside the array, velocities are much lower compared to those observed for the checkerboard pattern (c.f., Fig. 8e). In stark contrast to the checkerboard arrangement, the counter-clockwise Lorentz-forces along the magnet array lead to an intense global flow spanning a large volume as can be seen from the horizontal cut at $z = 10$ mm in Fig. 8h. Applied to multiple bubbles on an electrode this would mean that such a strong flow exerts drag forces on the bubbles acting mainly in electrode parallel direction. These drag forces could set the bubbles in sliding motion along the surface and support their earlier detachment.

Summary and conclusions

The aim of the current study was to investigate if the pressure change induced by the Lorentz-force-driven flow in an electrode-normal magnetic field can significantly alter the detachment process of an electrolytic gas bubble as suggested by Koza et al. [15]. In order to check this hypothesis the complex three-dimensional flow around a magnetized sphere ($d = 10$ mm), mimicking a gas bubble was measured by astigmatism particle tracking velocimetry. Finite volume computations complemented the experiments and were used to assess the pressure distribution around the bubble and the scaling of the flow-induced pressure change with the bubble diameter.

The comparison between the numerical simulation and the experiment shows a very good agreement. Based on the numerical simulations, it could be shown that the flow-induced lift force is minuscule for the low current densities used by Koza et al. [15]. Compared to bubble buoyancy this force is negligible and therefore unlikely to be the reason for the earlier bubble detachment. Moreover, scaling arguments and numerical results show that the flow-induced lift force and the buoyancy force both scale with the bubble diameter to the third power. Thus the ratio of both forces is expected to be of the same order of magnitude even for the small hydrogen bubbles characteristic for real systems and the conclusion drawn above should remain valid.

An alternative explanation for the observed detachment behavior might be sought in the collective effect of the Lorentz-force action around a group of bubbles. An array of magnets having parallel magnetization directions generates a similar force distribution if mounted directly below the electrode. The contributions of the single magnets, while almost canceling out inside the array, add up along the bounds of the array and drive a significant global rotational flow. The forces exerted on the bubbles by this flow may facilitate their detachment.

Acknowledgements

The financial support from DFG through the Emmy-Noether Research group program under grant No. CI 185/3 is gratefully acknowledged by JM, DB and CC. The authors would also like to thank K. Eckert, M. Uhlemann, G. Mutschke und J. Koza for fruitful discussions. TW appreciates productive discussions with V. Galindo concerning OpenFOAM.

REFERENCES

[1] Huggins RA. Energy storage: fundamentals, materials and applications. Springer; 2016.
[2] Ursua A, Gandia LM, Sanchis P. Hydrogen production from water electrolysis: current status and future trends. Proc IEEE 2012;100:410–26.
[3] Pletcher D, Li X. Prospects for alkaline zero gap water electrolysers for hydrogen production. Int J Hydrogen Energy 2011;36:15089–104.
[4] Zeng K, Zhang D. Recent progress in alkaline water electrolysis for hydrogen production and applications. Prog Energy Combust Sci 2010;36:307–26.
[5] Hine F, Yasuda M, Nakamura R, Noda T. Hydrodynamic studies of bubble effects on the iR-drops in a vertical rectangular cell. J Electrochem Soc 1975;122:1185–90.
[6] Bongenaar-Schlenter BE, Janssen LJJ, van Stralen SJD, Barendrecht E. The effect of the gas void distribution on the ohmic resistance during water electrolytes. J Appl Electrochem 1985;15:537–48.
[7] Dukovic J, Tobias CW. The influence of attached bubbles on potential drop and current distribution at gas-evolving electrodes. J Electrochem Soc 1987;134:331–43.
[8] Vogt H, Balzer R. The bubble coverage of gas-evolving electrodes in stagnant electrolytes. Electrochim Acta 2005;50(10):2073–9.
[9] Hine F, Murakami K. Bubble effects on the solution iR drop in a vertical electrolyzer under free and forced convection. J Electrochem Soc 1980;127(2):292–7.
[10] Sillen C. The effect of gas bubble evolution on the energy efficiency in water electrolysis. Ph.D. thesis. TU Eindhoven; 1983.
[11] Balzer BJ, Vogt H. Effect of electrolyte flow on the bubble coverage of vertical gas-evolving electrodes. J Electrochem Soc 2003;150:E11–6.
[12] Zhang D, Zeng K. Evaluating the behavior of electrolytic gas bubbles and their effect on the cell voltage in alkaline water electrolysis. Ind Eng Chem Res 2012;51:13825–32.
[13] Matsushima H, Iida T, Fukunaka Y. Observation of bubble layer formed on hydrogen and oxygen gas-evolving electrode in a magnetic field. J Solid State Electrochem 2012;16:617–23.
[14] Matsushima H, Iida T, Fukunaka Y. Gas bubble evolution on transparent electrode during water electrolysis in a magnetic field. Electrochim Acta 2013;100:261–4.
[15] Koza JA, Mühlenhoff S, Żabiński P, Nikrityuk P, Eckert K, Uhlemann M, et al. Hydrogen evolution under the influence of a magnetic field. Electrochim Acta 2011;56:2665–75.
[16] Iida T, Matsushima H, Fukunaka Y. Water electrolysis under a magnetic field. J Electrochem Soc 2007;154:E112–5.
[17] Diao Z, Dunne PA, Zangari G, Coey JMD. Electrochemical noise analysis of the effects of a magnetic field on cathodic hydrogen evolution. Electrochem Commun 2009;11:740–3.
[18] Kaya MF, Demir N, Albawabiji MS, Tas M. Investigation of alkaline water electrolysis performance for different cost effective electrodes under magnetic field. Int J Hydrogen Energy 2017;42(28):17583–92.
[19] Koza JA, Uhlemann M, Gebert A, Schultz L. Desorption of hydrogen from the electrode surface under influence of an external magnetic field. Electrochem Commun 2008;10:1330–3.
[20] Koza JA, Mühlenhoff S, Uhlemann M, Eckert K, Gebert A, Schultz L. Desorption of hydrogen from an electrode surface

under influence of an external magnetic field - in-situ microscopic observations. Electrochem Commun 2009;11:425–9.
[21] Baczyzmalski D, Weier T, Kähler CJ, Cierpka C. Near-wall measurements of the bubble- and lorentz-force-driven convection at gas-evolving electrodes. Exp Fluids 2015;56:162.
[22] Weier T, Landgraf S. The two-phase flow at gas-evolving electrodes: bubble-driven and lorentz-force-driven convection. Eur Phys J Special Top 2013;220:313–22.
[23] Klausner J, Mei R, Bernhard D, Zeng L. Vapor bubble departure in forced convection boiling. Int J Heat Mass Transf 1993;36:651–62.
[24] Duhar G, Colin C. Dynamics of bubble growth and detachment in a viscous shear flow. Phys Fluids 2006;18:077101.
[25] Liu H, Pan L, Huang H, Qin Q, Li P, Wen J. Hydrogen bubble growth at micro-electrode under magnetic field. J Electroanal Chem 2015;754:22–9.
[26] Baczyzmalski D, Karnbach F, Yang X, Mutschke G, Uhlemann M, Eckert K, et al. On the electrolyte convection around a hydrogen bubble evolving at a microelectrode under the influence of a magnetic field. J Electrochem Soc 2016;163:E248–57.
[27] Luo L, White HS. Electrogeneration of single nanobubbles at sub-50-nm-radius platinum nanodisk electrodes. Langmuir 2013;29(35):11169–75.
[28] Yang X, Karnbach F, Uhlemann M, Odenbach S, Eckert K. Dynamics of single hydrogen bubbles at a platinum microelectrode. Langmuir 2015;31:8184–93.
[29] Fernández D, Maurer P, Martine M, Coey JMD, Möbius ME. Bubble formation at a gas-evolving microelectrode. Langmuir 2014;30:13065–74.
[30] Fernández D, Martine M, Meagher A, Möbius ME, Coey JMD. Stabilizing effect of a magnetic field on a gas bubble produced at a microelectrode. Electrochem Comm 2012;18:28–32.
[31] Liu H, Pan L, Wen J. Numerical simulation of hydrogen bubble growth at an electrode surface. Can J Chem Eng 2016;94:192–9.
[32] Jackson JD. Klassische Elektrodynamik. DeGruyter; 2006.
[33] Knoepfel H. Magnetic fields. Wiley; 2000.
[34] Cierpka C, Segura R, Hain R, Kähler CJ. A simple single camera 3C3D velocity measurement technique without errors due to depth of correlation and spatial averaging for microfluidics, Measurement. Sci Technol 2010;21:045401.
[35] Cierpka C, Rossi M, Segura R, Kähler CJ. On the calibration of astigmatism particle tracking velocimetry for microflows. Meas Sci Technol 2011;22:015401.
[36] Kähler CJ, Scharnowski S, Cierpka C. On the resolution limit of digital particle image velocimetry. Exp Fluids 2012;52:1629–39.
[37] Raffel M, Willert C, Wereley S, Kompenhans J. Particle image velocimetry. Springer Verlag; 2007.
[38] Cierpka C, Lütke B, Kähler CJ. Higher order multi-frame particle tracking velocimetry. Exp Fluids 2013;54:1533.
[39] Weller HG, Tabor G, Jasak H, Fureby C. A tensorial approach to computational continuum mechanics using object-oriented techniques. Comput Phys 1998;12(6):620–31.
[40] Bödewadt U. Die Drehströmung über festem Grunde. Z für Angew Math Mech 1940;20:241–53.
[41] Irodov IE. Basic laws of electromagnetism. Mir; 1986.